

# Effect of Microstructure on the Thermal Conductivity of Plasma-Sprayed $\text{Al}_2\text{O}_3$ -YSZ Coatings

Xuemei Song, Ziwei Liu, Mingguang Kong, Yongzhe Wang, Liping Huang, Xuebin Zheng, and Yi Zeng

(Submitted December 10, 2015; in revised form January 17, 2016)

The microstructures of three atmospheric plasma-sprayed (APS)  $\text{Al}_2\text{O}_3$ - $\text{ZrO}_2$  coatings were investigated using x-ray diffraction, scanning electron microscopy, and transmission electron microscopy. The differences in the microstructures of the three  $\text{Al}_2\text{O}_3$ - $\text{ZrO}_2$  coatings, including their phase compositions, cracks, pores, grain sizes, and solid solutions, were analyzed in detail. A close relationship was observed between the thermal conductivities of the coatings and the microstructures, and the  $\text{Al}_2\text{O}_3$ -YSZ coatings with more spherical pores, fewer vertical cracks, and finer grains exhibited the lowest thermal conductivity of 0.91 W/m·K. Compared with YSZ coatings,  $\text{Al}_2\text{O}_3$ -YSZ coatings can exhibit lower thermal conductivity, which may be attributed to the formation of an amorphous phase, smaller grains, and  $\text{Al}_2\text{O}_3$ -YSZ solid solution.

**Keywords**  $\text{Al}_2\text{O}_3$ -YSZ coatings, atmospheric plasma spraying, microstructure, thermal conductivity

## 1. Introduction

Thermal barrier coatings (TBCs) have been widely used in advanced gas turbines to protect hot-section metal components from high temperatures, which improve the reliability and durability as well as efficiency of engines (Ref 1-3). TBCs typically consist of 6-8 wt.% yttria-stabilized zirconia (YSZ) deposited by atmospheric plasma spraying (APS) or electron beam physical vapor deposition (EB-PVD) because of its relatively high thermal expansion coefficient and low thermal conductivity (Ref 4-6). However, YSZ TBCs are approaching their durability and temperature limits because of the long-term accelerated sintering and phase transformations occurring above 1200 °C (Ref 7).

Currently, research in this field is increasingly focusing on the development of new TBC systems with higher temperature stability and lower thermal conductivity. Recently, several studies suggested  $\text{Al}_2\text{O}_3$ -YSZ coatings as potential candidates for TBC applications. In 2011, Tarasi et al. prepared  $\text{Al}_2\text{O}_3$ -YSZ coatings with good thermal stability at

high temperature (as high as 1500 °C) and lower thermal conductivity (0.99 W/m·K at room temperature) (Ref 8). Fabrication, microstructures and mechanical properties of  $\text{Al}_2\text{O}_3$ -YSZ coatings were also investigated (Ref 9-11). Bo Liang et al. found that the tribological behaviors of the  $\text{Al}_2\text{O}_3$ - $\text{ZrO}_2$  coatings prepared by APS were closely related to their physical and mechanical properties. For instance, a higher thermal conductivity of  $\text{Al}_2\text{O}_3$ -70 vol.%  $\text{ZrO}_2$  coatings can contribute to a better wear resistance by reducing the contact temperature and the thermal stress developed underneath the contact (Ref 9). J. Suffner et al. reported that the friction, wear properties, stiffness and bending strength of the as-sprayed materials of near-eutectic composition were superior to those obtained for non-stoichiometric  $\text{ZrO}_2$ - $\text{Al}_2\text{O}_3$  coatings produced by APS plus subsequent quenching with liquid nitrogen-cooled substrates (Ref 10). However, the relationship between the microstructure and low thermal conductivity of  $\text{Al}_2\text{O}_3$ -YSZ coatings has rarely been reported.

In this study,  $\text{Al}_2\text{O}_3$ -YSZ coatings with various thermal conductivities were deposited using APS, and the effects of the amorphous phase content, grain size, and crack distribution on the thermal conductivity are discussed.

## 2. Experimental Procedure

### 2.1 Preparation of Feedstock and Coatings

Nanosized  $\text{Al}_2\text{O}_3$  (55 wt.%) and YSZ (45 wt.%, 8 mol.% yttria-stabilized zirconia) powders (Jiangsu Lida Hi-Tech Special Material Co. Ltd, China) were mixed by milling as raw materials. Scanning electron microscopy (SEM) images of the nano- $\text{Al}_2\text{O}_3$  powders with sizes <50 nm and nano-YSZ powders with sizes with sizes

Xuemei Song, Ziwei Liu, Yongzhe Wang, and Yi Zeng, The State Key Lab of High Performance Ceramics and Superfine Microstructure, Shanghai Institute of Ceramics, Chinese Academy of Sciences, Shanghai 200050, China; Mingguang Kong, Key Laboratory of Materials Physics, Institute of Solid State Physics, Chinese Academy of Sciences, Hefei 230031, China; and Liping Huang and Xuebin Zheng, Key Laboratory of Inorganic Coating Materials, Shanghai Institute of Ceramics, Chinese Academy of Sciences, Shanghai 200050, China. Contact e-mail: zengyi@mail.sic.ac.cn.

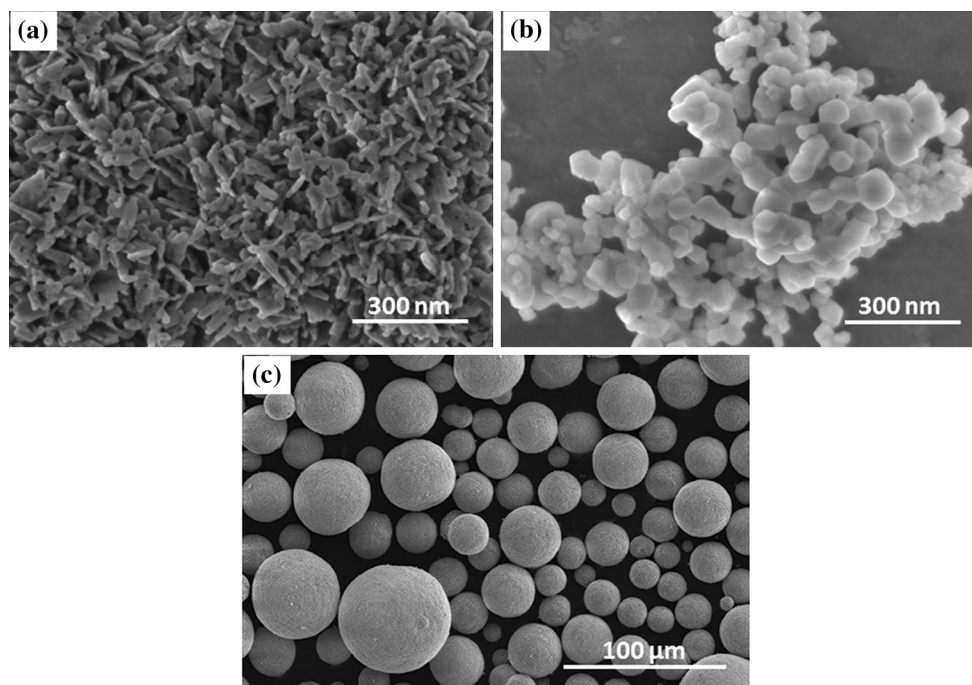


**Fig. 1** SEM images of raw materials: (a) nano- $\text{Al}_2\text{O}_3$  powders, (b) nano-YSZ powders, and (c)  $\text{Al}_2\text{O}_3$ -YSZ spray-dried powders

**Table 1** Operating parameters used for the APS process

Parameter	Values			Unit
Spraying condition	A	B	C	
Arc current	700	700	650	A
Primary plasma gas (Ar)	10	10	35	L/min
Secondary plasma gas ( $\text{H}_2$ )	15	15	15	L/min
Powder feed rate	10	10	10	r/prm
Spray distance	120	120	120	mm
Cooling medium	Compressed air	Water	Water	

<50 nm are presented in Fig. 1(a), (b). To ensure a high flowability for the APS system, the nanopowders were agglomerated into microsized, spherical particles ranging from 10 to 70  $\mu\text{m}$  in diameter by spray drying (as shown in Fig. 1c).

The  $\text{Al}_2\text{O}_3$ -YSZ coatings were fabricated using an A-2000 APS system equipped with a F4-MB plasma gun (Sulzer Metco AG, Switzerland) using three different sets of parameters, as listed in Table 1. The three spraying conditions were labeled A, B, and C.

Pieces of stainless steel ( $128 \times 85 \times 2 \text{ mm}^3$ ) were used as the substrates. Before the APS process, the surfaces of the substrates were grit blasted to allow for the deposition of well-adhered coatings. The deposited coatings were approximately 1.5 mm in thickness.

## 2.2 Characterization of Feedstock and Corresponding Coatings

The phase compositions of the coatings were identified using x-ray diffraction (XRD) (D8 ADVANCE, Bruker, Germany) using  $\text{Cu K}\alpha$  radiation. The XRD measurements were performed in the  $2\theta$  range of  $10^\circ$ - $80^\circ$  at a

scanning speed of  $4^\circ/\text{min}$ . The microstructure was also characterized using SEM (Magellan 400, FEI, USA) equipped with energy-dispersive x-ray spectroscopy (EDS) and electron backscattered diffraction (EBSD) (INCA SERIES, Oxford Instrument, UK) attachments and transmission electron microscopy (TEM) (JEM-2100F, JEOL, Japan).

## 2.3 Thermal-Conductivity Measurements

The deposited coatings were removed from the substrates to produce freestanding parts that could be used for thermal-conductivity tests. The freestanding coatings were then grinded and polished to a desired size for thermal diffusivity and specific heat capacity measurements. The thermal diffusivity ( $\alpha$ ) of the coatings was measured using the laser flash method, and the corresponding sample size was  $\Phi 10 \text{ mm} \times 0.9 \text{ mm}$ . The specific heat capacity ( $C_p$ ) of the coatings was measured using differential scanning calorimetry, and the corresponding sample size was  $\Phi 5.5 \text{ mm} \times 0.5 \text{ mm}$ . Their respective thermal-conductivity ( $\lambda$ ) values were then calculated from

their density ( $\rho$ ), as measured by the Archimedes method, using the following equation:

$$\lambda = C_p \cdot \alpha \cdot \rho \quad (\text{Eq 1})$$

YSZ (8 mol.% yttria-stabilized zirconia) coatings were also prepared by APS using the parameters as shown in Table 1, and their thermal conductivities were measured to compare to those of APS  $\text{Al}_2\text{O}_3$ -YSZ coatings.

### 3. Results and Discussion

#### 3.1 Microstructure of the Coatings

The phase compositions of the  $\text{Al}_2\text{O}_3$ -YSZ coatings deposited under the three different APS conditions were examined using XRD, and the results are presented in Fig. 2. A single broad halo peak corresponding to a fully amorphous phase was observed at  $2\theta = 20^\circ\text{--}40^\circ$  for coating A, which indicated that it is almost fully amorphous. In contrast, coatings B and C exhibited some diffraction peaks attributable to crystalline phases such as *c*- $\text{ZrO}_2$  and  $\alpha$ - $\text{Al}_2\text{O}_3$  in addition to an amorphous phase. However, there were more crystalline phases in coating C than in coating B, as indicated by the higher crystalline peak intensity in coating C. The formation mechanisms of the amorphous phase and crystalline phase in the  $\text{Al}_2\text{O}_3$ -YSZ coatings were explained in detail in our previous work (Ref 12). The differences in the phase composition among the three coatings were attributed to the different melting and mixing degrees of the in-flight particles and APS cooling rate in the different APS processes. Note that there was an obvious difference in the phase composition between coating A and coating B for the same APS parameters. The cooling methods can greatly affect the amorphous phase content. It is well known that the heat-transfer rate of a gas is faster than that of a liquid. Therefore, the higher cooling rate obtained for the compressed cooling substrate was more conducive to the for-

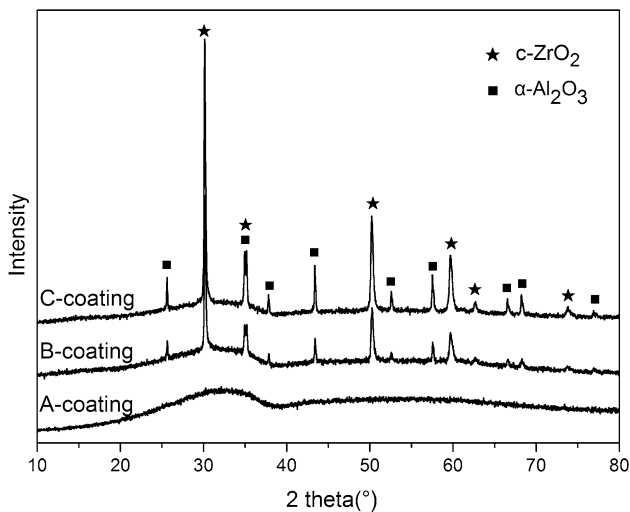


**Fig. 2** XRD patterns of the as-sprayed  $\text{Al}_2\text{O}_3$ -YSZ coatings under three different APS conditions. *c*- $\text{ZrO}_2$ : cubic YSZ;  $\alpha$ - $\text{Al}_2\text{O}_3$ : hexagonal alumina

mation of the amorphous phase in the preparation of coating A (compared to that of coating B).

Figure 3 presents backscattered electron SEM images of the polished cross sections of the as-sprayed  $\text{Al}_2\text{O}_3$ -YSZ coatings prepared using the three different APS conditions. The microstructure of the  $\text{Al}_2\text{O}_3$ -YSZ coatings consist of dense regions intermixed with pores, cracks, or unmelted particles. However, the three  $\text{Al}_2\text{O}_3$ -YSZ coatings exhibited different structural characteristics. Coating A contains many vertical cracks and some spherical pores (Fig. 3a and b). Coating B contains more horizontal cracks, more spherical pores, and fewer vertical cracks than coating A (Fig. 3c and d). In addition, some scattered grains were embedded in a dense matrix of coating B, which should contribute to the formation of crystalline phase peaks in XRD patterns of coating B. Compared with coatings A and B, a large number of partly melted or unmelted particles were observed in coating C (Fig. 3e and f). Formation mechanism of the different structural characteristics in  $\text{Al}_2\text{O}_3$ -YSZ coatings can be found in our previous works (Ref 12, 13).

TEM analysis was used to obtain more detailed information about the microstructure of the coatings, and the results are presented in Fig. 4, 5, and 6. In Fig. 4, the diffuse halo rings in the selected area electron diffraction (SAED) pattern indicate that coating A was mainly composed of an amorphous phase. Some amorphous phase was also observed in coating B, as indicated by Fig. 5(a), which was consistent with the broad halo peak spanning a  $2\theta$  range of  $20^\circ\text{--}40^\circ$  in the XRD patterns of coating B in Fig. 2. Figure 5(f) reveals that some scattered grains with sizes of 500 nm–1  $\mu\text{m}$  were embedded in the amorphous matrix of coating B, which may be the same as the scattered black and white grains observed in the SEM images of the cross section of coating B in Fig. 3(d). The formation of the grains may result from the growth of unmelted nano- $\text{Al}_2\text{O}_3$  and nano-YSZ grains. In addition, significant quantities of nanocrystals with irregular shapes and sizes  $<100$  nm were observed in coating B, as illustrated in Fig. 5(b)–(e). For instance, the diffuse rings in the SAED pattern of Fig. 5(b) and the magnified view of Fig. 5(b) presented in Fig. 5(c) confirm that coating B contained a large amount of a polycrystalline nanostructure. The nanostructure could be the result of the recrystallization during rapid solidification, which could contribute to the formation of the crystalline phase peaks in the XRD patterns of coating B. However, in addition to some structures similar to those in the coating B, the TEM results in Fig. 6 indicated that a large number of partly melted or unmelted grains existed in coating C, which is consistent with the SEM results in Fig. 3(e) and (f). The regular diffraction spots in the SAED patterns in Fig. 6(b) and (e) indicate that the dark grains were cubic zirconia single crystals and the light grains were hexagonal alumina single crystals. Furthermore, the single crystals were not pure  $\text{ZrO}_2$  or  $\text{Al}_2\text{O}_3$  but contained four chemical components of aluminum, zirconium, yttrium, and oxygen, as determined by EDS analysis and shown in Fig. 6(c) and (f), which may be attributed to the formation of  $\text{Al}_2\text{O}_3$ -YSZ solid solution. This solid solution has often



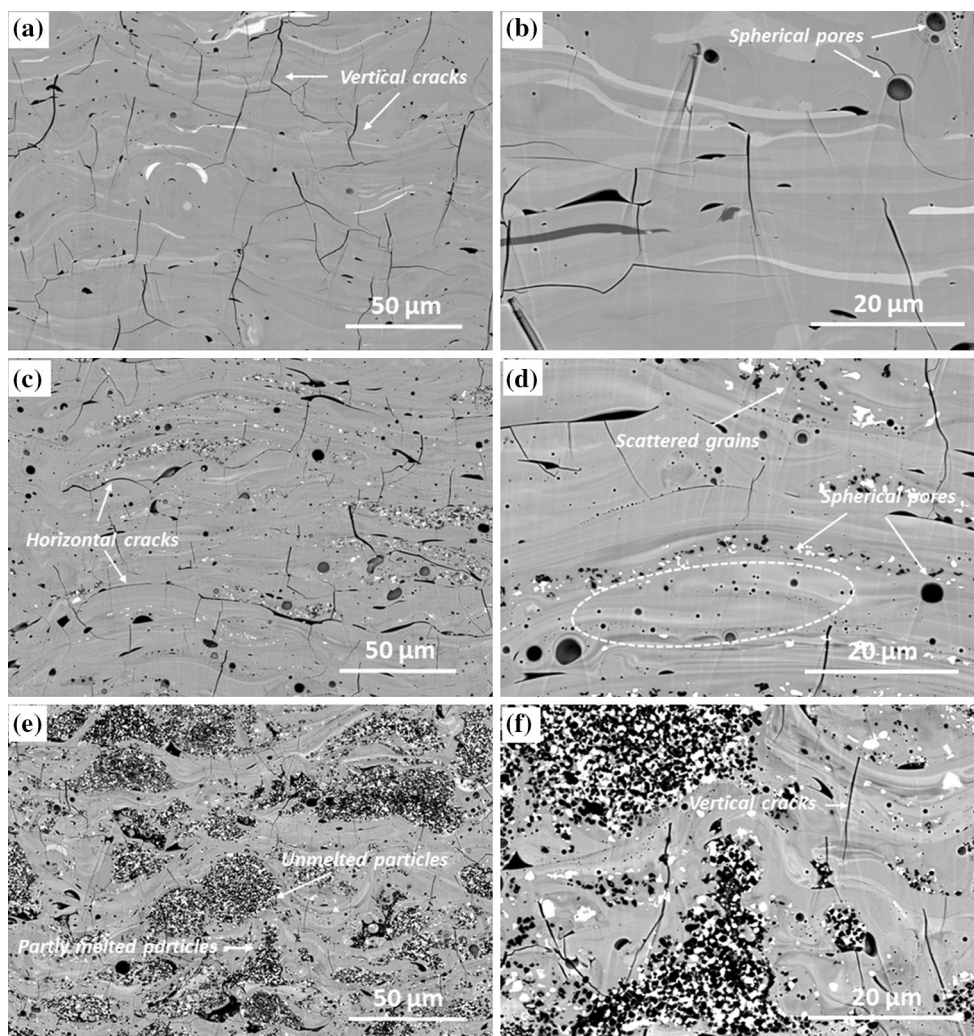


**Fig. 3** Backscattered electron SEM images of polished cross sections of the as-sprayed  $\text{Al}_2\text{O}_3$ -YSZ coatings under three different APS conditions: coatings (a, b) A; (c, d) B; and (e, f) C

been previously reported in  $\text{Al}_2\text{O}_3$ - $\text{ZrO}_2$  coatings (Ref 14).

### 3.2 Thermal Conductivity of the Coatings

The room-temperature thermal-conductivity measurement results of the three  $\text{Al}_2\text{O}_3$ -YSZ coatings are presented in Fig. 7. Comparison of the results suggests that coating B exhibits the lowest thermal conductivity of 0.91 W/m-K among the three coatings. For comparison, YSZ coatings were prepared using the same nano-YSZ powders shown in Fig. 1(b) as raw materials using the APS parameters as shown in Table 1. The lowest thermal conductivity reached by the YSZ coatings prepared by the parameter of coating C was 1.17 W/m-K, as shown in Fig. 7, which is higher than that of coating B. Furthermore, the thermal conductivity of coating B is lower than that of  $\text{Al}_2\text{O}_3$ -YSZ coatings reported in the literature (Ref 8).

Microstructure of the YSZ coating is also characterized by SEM equipped with the EBSD, as shown in Fig. 8.

Figure 8(a) shows the SEM image of polished cross section of YSZ coating. It is found that the microstructure of YSZ coating consists of dense regions intermixed with pores, cracks and unmelted particles. The EBSD result in Fig. 8(b) reveals that the dense regions are composed of submicron and micron-sized grains including columnar grains, equiaxed grains and large grains. Obviously, YSZ coating contains more pores and larger grains compared to coating B (Fig. 3c).

### 3.3 Relationship Between the Microstructure and Thermal Conductivity of the Coatings

To explain the differences among the thermal conductivities of the three  $\text{Al}_2\text{O}_3$ -YSZ coatings and between the  $\text{Al}_2\text{O}_3$ -YSZ coatings and YSZ coatings, the effect of the microstructure on the thermal conductivity of the  $\text{Al}_2\text{O}_3$ -YSZ coatings was analyzed in detail. As mentioned in section 3.1, the factors contributing to the different microstructures of the three  $\text{Al}_2\text{O}_3$ -YSZ coatings include

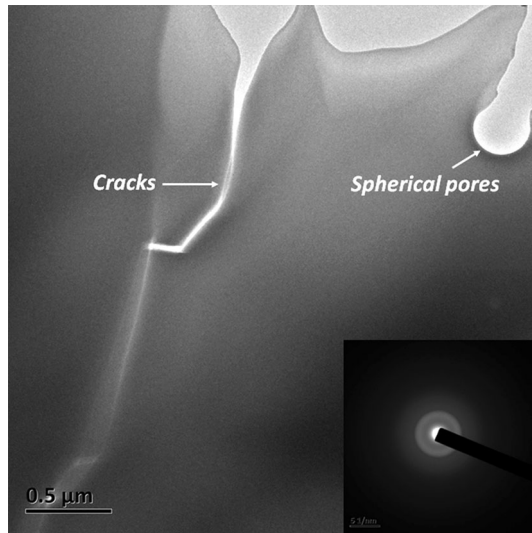


**Fig. 4** Brightfield TEM images and SAED patterns of a cross section from coating A

the phase composition, cracks, pores, grain size, and solid solution.

- (1) *Phase composition* The  $\text{Al}_2\text{O}_3$ -YSZ coatings consisted of an amorphous phase and crystalline phase. However, the amorphous phase content in the three  $\text{Al}_2\text{O}_3$ -YSZ coatings differed, and the coating A was fully amorphous. The thermal conductivity of a crystalline solid results from changes of lattice vibrations which are usually described in terms of phonons. The expression for the thermal conductivity derived by Debye is (Ref 15)

$$\lambda = \frac{1}{3} l_p C_v v \quad (\text{Eq 2})$$

where  $\lambda$  is the thermal conductivity,  $C_v$  is the specific heat,  $v$  is the phonon velocity, and  $l_p$  is the mean free path for scattering of phonons. Equation 2 reveals that the thermal conductivity values of the same material depend sensitively on  $l_p$ . An amorphous material exhibits a structure

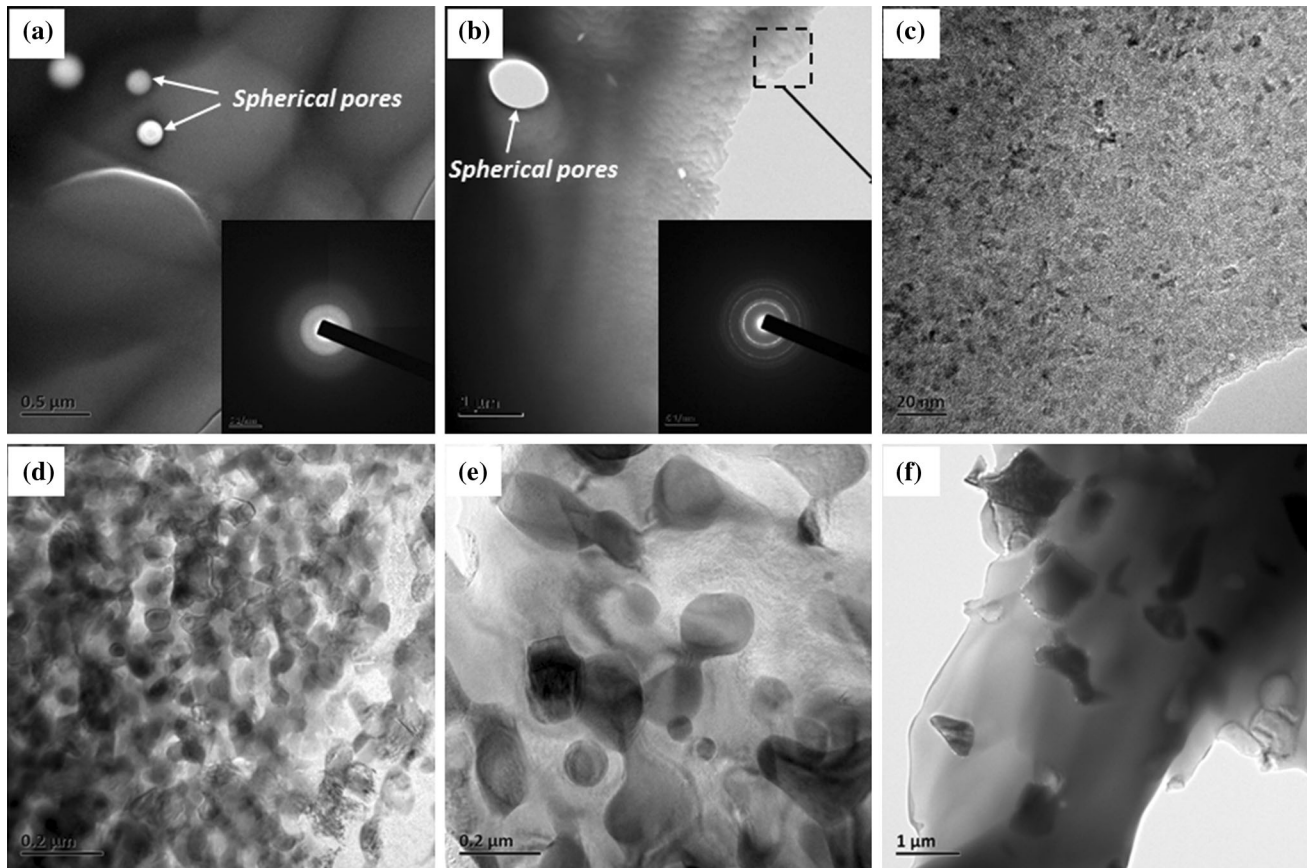


**Fig. 5** Brightfield TEM images and SAED patterns of a cross section from coating B



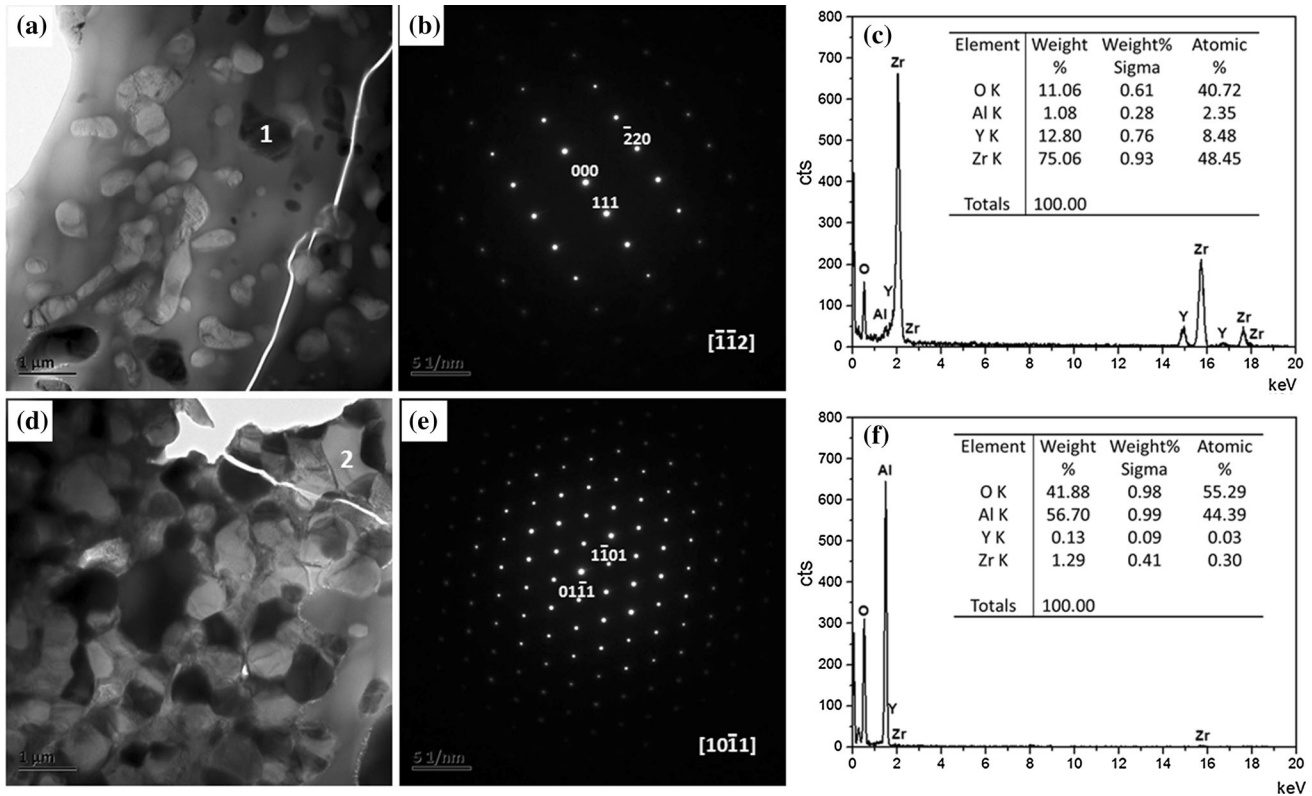


**Fig. 6** (a, d) Brightfield TEM images of a cross section from coating C; (b) SAED patterns corresponding to the  $c$ - $ZrO_2$  (cubic YSZ) using the  $[112]$  zone axis; (c) EDS profile of the dark grain (No. 1); (e) SAED patterns corresponding to the  $\alpha$ - $Al_2O_3$  (hexagonal alumina) using the  $[1011]$  zone axis; and (f) EDS profile for the bright grain (No. 2)

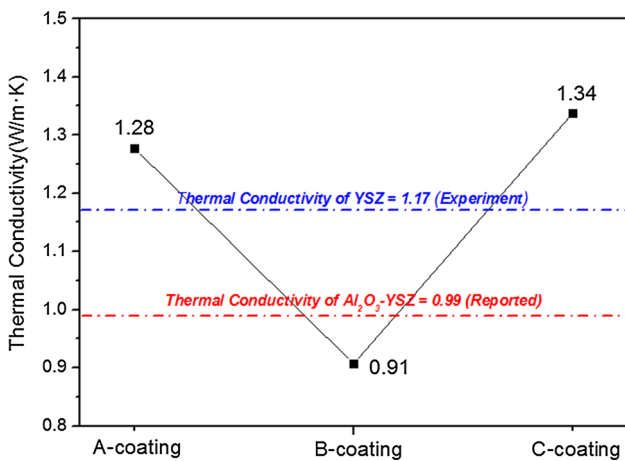


**Fig. 7** Thermal conductivity of the as-sprayed  $Al_2O_3$ -YSZ coatings and YSZ coating

with short-range order and long-range disorder. In terms of its heat conduction mechanism, an amorphous structure might be approximately regarded as a “crystal” composed of numerous, extremely fine grains with diameters of a few lattice spacings. The heat conduction mechanism of pho-

nons can be used to describe the heat conduction behavior of an amorphous material. The relevant literature indicates that the maximum of  $l_p$  corresponds to the diameter of the grain, which happens at low temperature, and the minimum of  $l_p$  corresponds to a few lattice spacings taking place at high temperature (Ref 15). Intense phonon collision leads to smaller  $l_p$  values with the increasing temperature. For normal crystals, the value of  $l_p$  decreases gradually from the diameter of the grain at low temperature to a few lattice spacings at high temperature with the increasing temperature. For an amorphous material, regarded as a “crystal” with extremely fine grains, the value of  $l_p$  at different temperatures is essentially constant (approximately a few lattice spacings). Therefore, the thermal conductivity of an amorphous phase at any temperature is lower than that of a crystalline phase for the same material. In theory, the thermal conductivity of the coating A should be the lowest of the three  $Al_2O_3$ -YSZ coatings; however, it is not, suggesting that other microstructural features have a significant effect on its thermal conductivity. The actual values of  $l_p$  depend sensitively on the interface, defects, and impurities, which lead to strong phonon scattering. Stronger phonon scattering results in a smaller value of  $l_p$ .

In addition, the amorphous phase may be the one reason for the thermal conductivity of coating B being lower than that of the YSZ coatings.

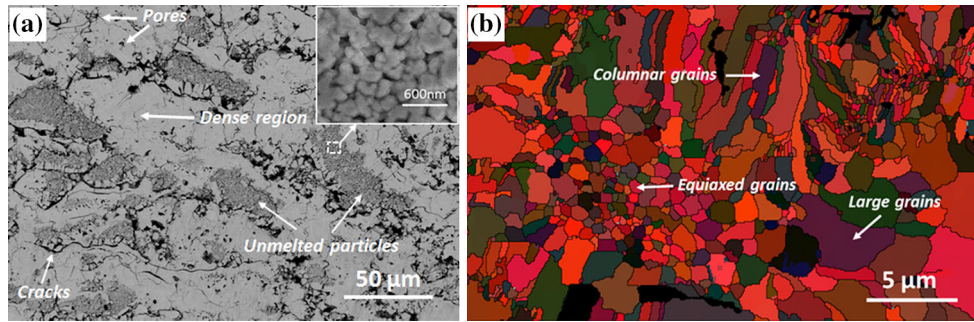


**Fig. 8** (a) SEM image of polished cross section of YSZ coating; (b) EBSD color-coded orientation map of a dense region in polished cross section of YSZ coating

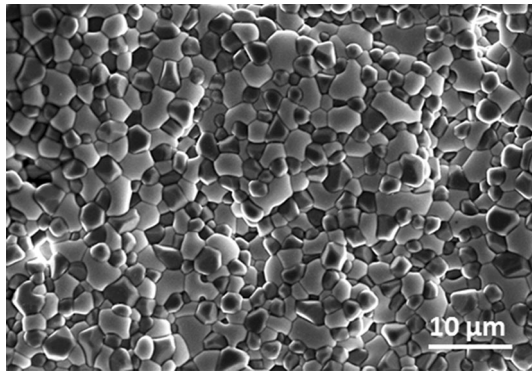


**Fig. 9** SEM image of the surface of the Al<sub>2</sub>O<sub>3</sub>-YSZ ceramic

(2) *Pores and cracks* Spherical pores and horizontal cracks (perpendicular to the direction of heat transfer) increase phonon scattering, leading to a decrease of thermal conductivity. However, vertical cracks (parallel to the direction of heat transfer) promote phonon heat transfer, leading to an increase of thermal conductivity. Hence, more spherical pores and fewer vertical cracks as shown in Fig. 3 result in coating B exhibiting a lower thermal conductivity than coating A with higher amorphous phase content.

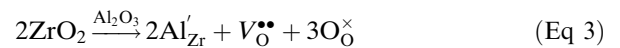
However, compared with coating B, more pores in the YSZ coating might not be enough to make it exhibit lower thermal conductivity, suggesting that other microstructural features also have significant influences on thermal conductivity.

(3) *Grain size* Grain boundaries are one of the important sources of phonon scattering. Smaller grain sizes result in larger grain densities, stronger phonon scattering, and lower thermal conductivity. According to the microstructural analysis in section 3.1, the crystalline phase in coating B is primarily composed of nanocrystals with irregular shapes and sizes <100 nm from the recrystallization, whereas the crystalline phase in coating C mainly consists of 500 nm<sup>-1</sup> μm grains resulting from

the growth of unmelted nano-Al<sub>2</sub>O<sub>3</sub> and nano-YSZ grains. Therefore, it is apparent that the average grain size of coating C is the largest in the three Al<sub>2</sub>O<sub>3</sub>-YSZ coatings when their amorphous phase is regarded as a special “crystal” composed of extremely fine grains with diameters of a few lattice spacings, which explains why coating C exhibits the highest thermal conductivity. To further confirm this hypothesis, an Al<sub>2</sub>O<sub>3</sub>-YSZ ceramic was sintered at 1700 °C for 2 h using the same Al<sub>2</sub>O<sub>3</sub>-YSZ spray-dried powders shown in Fig. 1(b) as raw materials. Figure 9 presents an SEM image of the surface of the Al<sub>2</sub>O<sub>3</sub>-YSZ ceramic. The microstructure of the Al<sub>2</sub>O<sub>3</sub>-YSZ ceramic is similar to that of the partly melted or unmelted particles in coating C shown in Fig. 6(d). The average grain size of the Al<sub>2</sub>O<sub>3</sub>-YSZ ceramic is 2.6 μm and its thermal conductivity is 7.87 W/m·K, which are much higher than those of coating C.

In addition, smaller grain size may be another factor resulting in the reduction of thermal conductivity of coating B compared to that of the YSZ coating.

(4) *Solid solution* According to the above analysis, an Al<sub>2</sub>O<sub>3</sub>-YSZ solid solution often appears in Al<sub>2</sub>O<sub>3</sub>-YSZ coatings. The formation of a solid solution is often accompanied by vacancies, solutes, and a local strain field, which can reduce  $l_p$  (Ref 15). For example, a defect chemistry in Al<sub>2</sub>O<sub>3</sub>-YSZ coatings can be represented using the following equation:



$\text{Al}'_{\text{Zr}}$ , which represents an Al<sup>3+</sup> cation that occupies a Zr<sup>4+</sup> cation site,  $\text{V}_\text{O}^{\bullet\bullet}$  is a doubly charged (positive) oxygen vacancy, and  $\text{O}_\text{O}^\times$  is an O<sup>2-</sup> anion on an oxygen site (neutral charge). The strain field and vacancies can increase the discrete degree of phonons in the lattice when they interact with scattering phonons. The increase of the discrete degree provides more chances of scattering between phonons, which will further reduce the mean free path for the phonons. Therefore, the formation of the Al<sub>2</sub>O<sub>3</sub>-YSZ solid solution may be the third factor resulting in the reduction of the thermal conductivity of coating B compared to that of the YSZ coatings.



## 4. Conclusions

Three  $\text{Al}_2\text{O}_3$ -YSZ coatings with different microstructures were prepared using APS. The thermal conductivities of the coatings were closely related to their microstructures. The factors contributing to the different microstructures of the three  $\text{Al}_2\text{O}_3$ -YSZ coatings included the phase composition, grain size, and the presence of cracks, pores, and a solid solution. The amorphous phase content and presence of horizontal cracks, spherical pores, nanocrystals, and a solid solution caused the  $\text{Al}_2\text{O}_3$ -YSZ coatings to exhibit low thermal conductivity by reducing the mean free path for phonon scattering. In contrast, the presence of vertical cracks and larger grains increased the thermal conductivity of the coatings by increasing the mean free path for phonon scattering. Thus, the coating containing more spherical pores, fewer vertical cracks, and finer grains exhibited the lowest thermal conductivity of 0.91 W/m·K among the three  $\text{Al}_2\text{O}_3$ -YSZ coatings. The formation of an amorphous phase, smaller grains, and solid solution in the  $\text{Al}_2\text{O}_3$ -YSZ coatings may also have contributed to the reduced thermal conductivity of this coating compared to that of the YSZ coating.

## Acknowledgments

Financial support for this study was provided by the Research Project Fund of the International Science & Technology Cooperation Project of China (2013DFG52290), Science & Technology Innovation Key Project of Shanghai Institute of Ceramics (Y37ZC4141G), Shanghai Technical Platform for Testing and Characterization on Inorganic Materials (14DZ2292900) and the CAS Key Technology Talent Program.

## References

1. R.A. Miller, Current Status of Thermal Barrier Coatings: An Overview, *Surf. Coat. Technol.*, 1987, **30**(1), p 1-11

2. N.P. Padture, M. Gell, and E.H. Jordan, Thermal Barrier Coatings for Gas-Turbine Engine Applications, *Science*, 2002, **296**(5566), p 280-284
3. S.O. Chwa and A. Ohmori, Microstructures of  $\text{ZrO}_2$ -8wt.% $\text{Y}_2\text{O}_3$  Coatings Prepared by a Plasma Laser Hybrid Spraying Technique, *Surf. Coat. Technol.*, 2002, **153**(2-3), p 304-312
4. W. Beele, G. Marijnissen, and A.V. Lieshout, The Evolution of Thermal Barrier Coatings Status and Upcoming Solutions for Today's Key Issues, *Surf. Coat. Technol.*, 1999, **121**, p 61-67
5. D. Stöver, G. Pracht, H. Lehmann, M. Dietrich, J.E. Döring, and R. Vaßen, New Material Concepts for the Next Generation of Plasma-Sprayed Thermal Barrier Coatings, *J. Therm. Spray Technol.*, 2004, **13**(1), p 76-83
6. B. Saruhan, P. Francois, K. Fritscher, and U. Schulz, EB-PVD Processing of Pyrochlore-Structured  $\text{La}_2\text{Zr}_2\text{O}_7$ -Based TBCs, *Surf. Coat. Technol.*, 2004, **182**(2-3), p 175-183
7. D. Basu, C. Funke, and R.W. Steinbrech, Effect of Heat Treatment on elastic properties of separated thermal barrier coatings, *J. Mater. Res.*, 1999, **14**(12), p 4643-4650
8. F. Tarasi, M. Medraj, A. Dolatabadi, J. Oberste-Berghaus, and C. Moreau, High-Temperature Performance of Alumina-Zirconia Composite Coatings Containing Amorphous Phases, *Adv. Funct. Mater.*, 2011, **21**(21), p 4143-4151
9. B. Liang, G. Zhang, H.L. Liao, C. Coddet, and C.X. Ding, Friction and Wear Behavior of  $\text{ZrO}_2$ - $\text{Al}_2\text{O}_3$  Composite Coatings Deposited by Air Plasma Spraying: Correlation with Physical and Mechanical Properties, *Surf. Coat. Technol.*, 2009, **203**(20-21), p 3235-3242
10. J. Suffner, H. Sieger, H. Hahn, S. Dosta, I.G. Cano, J.M. Guilemany, P. Klimczyk, and L. Jaworska, Microstructure and Mechanical Properties of Near-Eutectic  $\text{ZrO}_2$ -60 wt.%  $\text{Al}_2\text{O}_3$  Produced by Quenched Plasma Spraying, *Mater. Sci. Eng. A*, 2009, **506**(1-2), p 180-186
11. I. Zukerman, V.N. Zhitomirsky, G. Beit-Ya'akov, R.L. Boxman, A. Raveh, and S.K. Kim, Vacuum Arc Deposition of  $\text{Al}_2\text{O}_3$ - $\text{ZrO}_2$  Coatings: Arc Behavior and Coating Characteristics, *J. Mater. Sci.*, 2010, **45**(23), p 6379-6388
12. X.M. Song, T. Suhonen, T. Varis, L.P. Huang, X.B. Zheng, and Y. Zeng, Fabrication and Characterization of Amorphous Alumina-Yttria-Stabilized Zirconia Coatings by Air Plasma Spraying, *J. Therm. Spray Technol.*, 2014, **23**(8), p 1302-1311
13. X.M. Song, T. Suhonen, C. Sun, L.P. Huang, X.B. Zheng, and Y. Zeng, Microstructures, Microhardness, and Crystallization Behaviors of Amorphous  $\text{Al}_2\text{O}_3$ -YSZ Coatings Prepared by Air Plasma Spraying, *Surf. Rev. Lett.*, 2015, **22**(3), p 1550047
14. A.L. Vasiliev, N.P. Padture, and X.Q. Ma, Coatings of Metastable Ceramics Deposited by Solution-Precursor Plasma Spray: I. Binary  $\text{ZrO}_2$ - $\text{Al}_2\text{O}_3$  System, *Acta Mater.*, 2006, **54**(18), p 4913-4920
15. T.G. Xi, *Thermophysical Properties of Inorganic Materials*, Shanghai Science and Technology Press, Shanghai, 1981